

Carbon diffusion paths and segregation at high-angle tilt grain boundaries in α -Fe studied by using a kinetic activation-relation technique

Oscar A. Restrepo,^{1,2} Normand Mousseau,¹ Mickaël Trochet,¹ Fedwa El-Mellouhi,³
Othmane Bouhali,² and Charlotte S. Becquart⁴

¹*Département de physique and Regroupement québécois sur les matériaux de pointe, Université de Montréal,
Case postale 6128, succursale centre-ville, Montréal (QC) Canada H3C 3J7*

²*Texas A&M University at Qatar, Doha, Qatar*

³*Qatar Environment and Energy Research Institute, Hamad Bin Khalifa University, Doha, Qatar*

⁴*Université de Lille, CNRS, INRA, ENSCL, UMR 8207, UMET, Unité Matériaux et Transformations, F 59 000 Lille, France*



(Received 6 June 2017; revised manuscript received 7 October 2017; published 14 February 2018)

Carbon diffusion and segregation in iron is fundamental to steel production but is also associated with corrosion. Using the kinetic activation-relaxation technique (k-ART), a kinetic Monte Carlo (KMC) algorithm with an on-the-fly catalog that allows to obtain diffusion properties over large time scales taking into account long-range elastic effects coupled with an EAM force field, we study the motion of a carbon impurity in four Fe systems with high-angle grain boundaries (GB), focusing on the impact of these extended defects on the long-time diffusion of C. Short and long-time stability of the various GBs is first analyzed, which allows us to conclude that the $\Sigma 3(111)\theta = 109.53^\circ(110)$ GB is unstable, with Fe migration barriers of ~ 0.1 eV or less, and C acts as a pinning center. Focusing on three stable GBs, in all cases, these extended defects trap C in energy states lower than found in the crystal. Yet, contrary to general understanding, we show, through simulations extending to 0.1 s, that even though C diffusion takes place predominantly in the GB, it is not necessarily faster than in the bulk and can even be slower by one to two orders of magnitude depending on the GB type. Analysis of the energy landscape provided by k-ART also shows that the free cavity volume around the impurity is not a strong predictor of diffusion barrier height. Overall, results show rather complex diffusion kinetics intimately dependent on the local environment.

DOI: [10.1103/PhysRevB.97.054309](https://doi.org/10.1103/PhysRevB.97.054309)

I. INTRODUCTION

Diffusion and segregation of C atoms in Fe are associated with many complex kinetic processes that impact steel fabrication, catalysis, corrosion, or design of fission reactors, etc. [1–6]. These mechanisms have been studied extensively in crystalline bulk [7–11]. C diffusion in grain boundaries (GB), however, has received much less attention [12,13] and relatively little information is available regarding associated C diffusion mechanisms and pathways due, in large part, to the complexity of the environment.

This complexity means that diffusion and segregation at GBs are best studied, from a theoretical point of view, by computer simulations that can capture strain and conformation details, providing a rich microscopic picture [14–16]. For example, *ab initio* simulations have shown that S impurities in Ni could cause embrittlement by segregating at GBs, concentrating and weakening the metal bonding due to the stresses produced, a process known as GB decohesion [17,18]. In contrast, C atoms at GBs may enhance cohesion in Fe [16]. An extensive study of more than 170 Fe GB structures obtained by molecular static simulations at 0 K and presented as a function of the misorientation angle [19] finds that both low- and high-angle GBs are effective sinks for point defects. The formation energies show a dependence on the local atomic structure and the distance from the boundary center. Due to the static nature of that work, this impressive analysis of the

GB morphologies as a function of the misorientation angle leaves, nevertheless, many questions open. For example, it does not provide information on how morphologies correlate with dynamical properties and diffusion paths of interstitials, what the specific diffusion mechanisms are, and what to expect as to dynamical behavior for high-angle GBs, which is much more complicated than for low-angle GBs.

It is generally believed that diffusion is faster at GBs than in the bulk [13,20,21] and that GBs can dominate mass transport at low and medium temperatures, as they provide rapid diffusion paths for C in iron. This view is supported both by C diffusion experiments—that find a C diffusion coefficient three to four orders of magnitude greater at GBs than in the lattice using autoradiography—[13] and by continuum theory [20,21]—that supposes a GB to be an open flat region with a δ separation between grains, neglecting the particular topologies and interactions in it. These observations are supported by recent MD simulations that suggest that dislocations at GBs behave like pipes and accelerate the diffusion of carbon [22]. MD simulations of C diffusion in bcc-Fe edge dislocation also predict migration barriers 0.3–0.4 eV lower than in the lattice as well as significant segregation caused by a trapping energy of 0.96 eV [23]. Nevertheless, the role of GBs in impurity diffusion was recently questioned by Teus *et al.* with new experiments and simulations [12]. In that work, authors conclude that both C and H atoms diffusing in bcc-Fe display a higher activation enthalpy for migration in the GBs than in the

bulk, indicating that GBs in bcc-Fe act as traps for interstitial atoms, thus retarding their diffusion. A similar conclusion was derived from another work for H diffusion in pure bulk bcc-Fe [24]. The controversy not only involves bcc metals but fcc metals as well. For example, some works show H diffusion to be faster at Ni-GBs than in bulk [25–28], while others indicate that, depending on several factors such as the grain size, the GB energy, angle, the probability of GB connectivity, and the excess of free volume, H diffusion can also be slower [29]. Similarly, KMC simulations of H diffusion in Al predict that H diffusion along GBs is reduced by more than one order of magnitude compared with the crystal [30].

Recently, an extensive quantification at atomic-scale of GB segregation of C in iron was performed using a combination of atom probe tomography for the chemical sensitivity with transmission electron microscopy for accurate structural characterization [31]. Measuring a total of 121 GBs, the authors confirmed the presence of a linear trend between carbon segregation and the misorientation angle for low-angle GBs (lower than 15°), but did not find any general tendency for high-angle GBs. This conclusion is consistent with the theoretical results of Ref. [19], as at high-angles, the GB plane and rotation axis play only a secondary role because of the wide range of local topologies formed in these GBs. Although the particular geometry of GB topologies can be explained at a first approximation by the structural unit model [32–34], a correct description of the diffusion paths and segregation requires a specific analysis. Such analysis is challenging because of the large diversity of topologies formed at GBs, which can generate a diversity of pathways with characteristic time scales that are often out of reach of standard atomistic simulation techniques.

To fully conclude this debate, a complete characterization of the potential energy landscape associated with the diffusion pathways at GBs is still required, to ensure that the conclusions from high temperature simulations or based on a limited set of mechanisms hold everywhere. In this paper, we use the kinetic activation-relation technique (k-ART), an off-lattice kinetic Monte Carlo (KMC) method with on-the-fly catalog generation [35–37], to fully characterize the energy landscape and long-time diffusion pathways of carbon at four representative GBs in bcc-Fe. After presenting the methodology and sample construction, we assess the stability of the various GBs using MD and KMC over short (nanosecond) time scales. The subsequent section assesses GB stability over large (up to millisecond) time scales. A full study of C diffusion is then performed on the three stable systems using k-ART only, providing a detailed characterization of the energy landscapes and kinetics.

II. METHODOLOGY

We focus here on the long-time dynamical properties of C impurities in the presence of GBs. More specifically, we initially consider four representative systems for which static properties have already been characterized numerically elsewhere [19]. We first assess their dynamical properties over short (nanosecond) time scales with MD, using LAMMPS [38,39] and, over longer time scales (up to seconds and years), with the k-ART code [35–37].

A. K-ART implementation

K-ART is a kinetic Monte Carlo algorithm with on-the-fly event catalog building capacity and exact treatment of elasticity. Before each KMC step, it identifies new environments based on their local topology. If these topologies are already present in the catalog, associated events are inserted in the event tree, otherwise, unbiased open-ended searches for transition states and new minima are launched, using the activation-relaxation technique (ART nouveau) [40–42]. Each of these events is ranked according to a rate given by transition state theory, $r_i = \nu e^{-E_b/k_B T}$, where ν is a fixed prefactor, set to the Debye frequency of 10^{13} s^{-1} , k_B is the Boltzmann's constant, T is the temperature, and E_b is the barrier energy defined as the energy difference between the transition state and the initial minimum [43–45]. Once the event tree is completed, all events with an occurrence probability greater or equal to 1 in 10000 are reconstructed and their transition state fully relaxed to account for the elastic deformations. Following standard KMC rules [46], the time step, if the system is not trapped in flickers (see below), is chosen according to a Poisson distribution as $\Delta t = -\ln(\mu) / \sum_i r_i$, where μ is a random number.

To classify configurations, k-ART generates a local connectivity graph that involves each atom and their local surrounding. Here, we use a cutoff of 2.7 \AA for drawing a link between two atoms and a radius of 6.0 \AA around the central atom for the maximum graph size. Graphs are then analyzed using the NAUTY code, a topological analysis package that provides a unique identifier associated with the graph's automorphic group as well as the permutations allowing to restore the reference graph [47,48]. This classification makes it possible to construct a unique catalog for any environment with reference to crystalline lattice, including alloys and glasses. Here, k-ART can handle configurations and events with any level of disorder at the GBs effortlessly.

Interactions are handled using the Fe-C EAM potential developed by Becquart *et al.* for Fe-C [49,50] and Ackland and Mendeleev for Fe-Fe interactions [51]. Both potentials provide an excellent agreement with DFT calculations in bulk Fe [7,50]. K-ART is coupled to LAMMPS library for force and energy calculations [38,39]. The MD part of LAMMPS is also used for getting the dynamics of the first nanosecond in all calculations.

B. Computation of energies and square displacement

In what follows, we generally measure energy with respect to the lowest-energy state found during each simulation, which defines the ground state (GS). Energies for specific states are therefore indicated as $\delta E = E - E_{\text{GS}}$.

The segregation energy is defined as the difference between the system's energy with the C atom located at the GB, and that located in the perfect lattice,

$$E_s = (E_{\text{min}}^{\text{1C}} - E_{\text{min}}^0) - (E_{\text{lat}}^{\text{1C}} - E_{\text{lat}}^0),$$

with $(E_{\text{lat}}^{\text{1C}} - E_{\text{lat}}^0) = -10.058 \text{ eV}$. Here, E_{min}^0 and E_{lat}^0 correspond to the minimized energies of GB system and perfect lattice without the C atom and, $E_{\text{lat}}^{\text{1C}}$ is the energy of the perfect lattice with a C interstitial. The unique variable is the minimum energy found at each KMC step $E_{\text{min}}^{\text{1C}} = E_{\text{min}}$

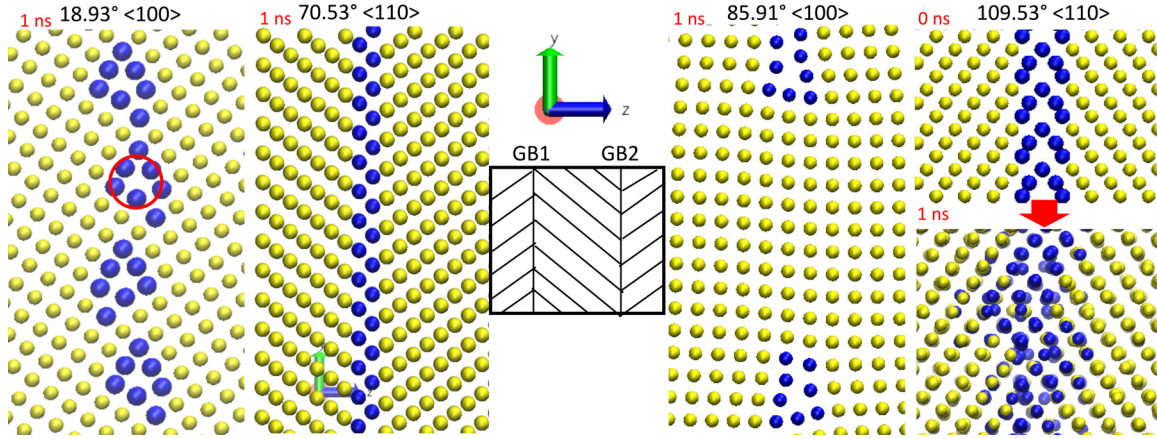


FIG. 1. Details of the GB topologies after 1 ns of MD used for k-ART simulations and at the center, a general sketch of the four boxes. In blue, atoms with different structure from bcc at GB and in yellow, Fe atoms with crystalline structure. The GB rotation axes $\langle 100 \rangle$ and $\langle 110 \rangle$ are parallel to the x axis out of planes, while GB planes are perpendicular to the z axis. The red circle indicates a large free volume in the $18.93^\circ \langle 100 \rangle$ GB, in which the Fe atoms represented in blue jump back and forth; this is also the ground state of a C atom.

(super index suppressed for simplicity). Equivalently, $E_s = E_{\min} - E_0$ (where E_0 is the initial energy of the GB system with the C interstitial at the center, in a crystalline site). The segregation energy is the opposite of the binding energy, and a lower segregation energy indicates that the C atom has a higher tendency to bind to the GB. The GB energy, E_{GB} , that represents the energy change caused by the presence of the GB is calculated as

$$E_{\text{GB}} = \frac{E_{\min}^0 - E_{\text{lat}}^0}{2A},$$

where A is the area of the GB plane (the 2 comes from the fact that there are two GBs in the simulation box). The activation energy for an event is defined as the energy difference between the initial minimum E_{\min} and the saddle E_{sadd} (i.e., the barrier crossed between two adjacent minima) or

$$E_b = E_{\text{sadd}} - E_{\min}.$$

Moreover, we define as the effective barrier, the total barrier crossed when jumping from one GS to another GS. Finally, the square displacement SD is computed as usual,

$$SD = \sum_{i=1}^N (\mathbf{r}_i(t_n) - \mathbf{r}_i(0))^2,$$

where N is the number of particles and $\mathbf{r}_i(t_n)$ is the position of atom i at KMC step n . No normalization to N is done, since diffusion is totally dominated by the motion of the defects or their neighboring atoms, with the majority of the atoms remaining at their initial position.

C. Configurations setup

Our simulations focus on four different GBs in cells with periodic boundary conditions. Each is based on crystalline bcc-Fe with a lattice parameter $a_0 = 2.8553 \text{ \AA}$. Because of the periodic conditions, all configurations have two symmetric tilt GBs with $\langle 100 \rangle$ or $\langle 110 \rangle$ axis of rotation parallel to the GB plane and high-angle boundaries with misorientations larger than 15° .

More exactly, the first two samples are of the $\langle 100 \rangle$ family, and of type $\Sigma 37(160)\theta = 18.93^\circ$ and $\Sigma 3140(54580)\theta = 85.91^\circ \approx \Sigma 421(14150)\theta = 86.05^\circ$, while the other two are of the $\langle 110 \rangle$ family, and of type $\Sigma 3(112)\theta = 70.53^\circ$ and $\Sigma 3(111)\theta = 109.53^\circ$ symmetric tilt GBs.

To facilitate comparison with literature, cells with GBs are taken from Ref. [15]. The box dimensions for the first model, $18.93^\circ \langle 100 \rangle$, are $17.140 \times 51.878 \times 51.686 \text{ \AA}^3$ with 3924 atoms; for the second model, $70.53^\circ \langle 110 \rangle$, $36.318 \times 34.557 \times 37.367 \text{ \AA}^3$ with 4032 atoms; for the third, $85.91^\circ \langle 100 \rangle$, $34.332 \times 113.090 \times 76.595 \text{ \AA}^3$ with 25537 atoms; and the last model, $109.53^\circ \langle 110 \rangle$, has $36.405 \times 34.977 \times 62.638 \text{ \AA}^3$ with 6840 atoms. The two GBs are separated by a distance equal to half the box size in the z direction. An atomistic representation of the GB of these models is shown in Fig. 1. As discussed below, in spite of the relatively large cell size, slowly decaying long-range interactions between GBs create a low-level strain throughout the cell, slightly affecting energy minima and energy barriers even in the farthest points from the GB. Since these effects are on the order of kT , however, they do not affect the overall conclusions of this work, especially near GB where the contributions of local strains are much larger than long-range ones.

The $18.93^\circ \langle 100 \rangle$ and $85.91^\circ \langle 100 \rangle$ structures are general GBs with medium and low energy E_{GB} (see Table I and Fig. 2 of Ref. [19]). They have been chosen because of their particular

TABLE I. GB energies per unit area, $E_{\text{GB}} = (E_{\min}^0 - E_{\text{lat}}^0)/2A$. (h, k, l) is the direction of the GB plane perpendicular to the rotation (axis) along the x direction.

GB (angle (axis))	$\Sigma(h, k, l)$	$E_{\text{GB}}(\text{meV}/\text{\AA}^2)$
$18.93^\circ \langle 100 \rangle$	37(1 6 0)	61.053
$85.91^\circ \langle 100 \rangle$	$3140(54580) \approx 421(14150)$	37.118
$70.53^\circ \langle 110 \rangle$	3(1 1 2)	16.223
$109.53^\circ \langle 110 \rangle$	3(1 1 1)	81.739

“structural units” and the free volumes available as C atoms should be trapped at these sites for longer periods of time. The $70.53^\circ \langle 110 \rangle$ and $109.53^\circ \langle 110 \rangle$ GBs have been chosen because they both are $\Sigma 3$ GBs with different misorientation angles. The $70.53^\circ \langle 110 \rangle$ GB is also extensively studied experimentally [52] due to its single structural unit that leads to a sharp minimum in the grain boundary energy, in contrast to the $109.53^\circ \langle 110 \rangle$ GB, which has one of the highest energy (Fig. 2 of Ref. [19]), as seen in Table I.

D. Handling flickering states

To avoid the well-known flickering problem produced by low energy barriers that can slow the KMC simulations almost to a grind, we use the basin autoconstructing mean rate method (bac-MRM) to solve analytically the average residence time for the in-basin states. This method computes on-the-fly a statistically exact analytic solution of the connected flickering states and their escape rate as the energy landscape is explored, at the cost of specific trajectories [36,53,54]. The bac-MRM is applied to all states connected by barriers and energy difference lower than a predefined threshold.

Flickering in basin states were handled as follows. For the $18.93^\circ \langle 100 \rangle$ GB, an initial threshold of 0.2 eV was set to define basins. Once the landscape for events around this energy was well established, the threshold was raised to 0.4 eV and further to 0.8 eV, in order to complete sampling of diffusion pathways. A similar step-by-step procedure was used for the two other main GBs, ensuring that the landscape around an energy level was fully understood before raising the threshold, from 0.4 to 0.6 eV and 0.8 eV, in the case of the $70.53^\circ \langle 110 \rangle$ GB, and 0.4, 0.5, and 0.8 eV for $85.91^\circ \langle 100 \rangle$ GB. As explained below, because of fundamental instabilities, the $109.53^\circ \langle 110 \rangle$ GB was not used in long-time k-ART simulations.

III. RESULTS

All simulations presented in this section are performed at a fixed temperature of 600 K, as this is the threshold temperature for phenomena such as corrosion initiation [55,56]. Since the energy landscape is temperature independent when barriers are high with respect to temperature, this choice only affects the kinetic part of the results, not the event catalog.

A. Stability of the grain boundaries over short time scales

A 1.0-ns run using MD-LAMMPS implementation in the NVT ensemble is performed for each pure Fe system before launching k-ART simulations in order to assess the short-time stability of the GBs and to eliminate any low Fe barriers. These low Fe barriers are due to the presence of small stresses and other factors linked to the construction of GBs and can reduce the time steps at the beginning of a k-ART run.

After 1.0 ns, we confirm that the three lowest angle-GBs are stable. In contrast, the $109.53^\circ \langle 110 \rangle$ GB deforms considerably and shows clear instability (compare frames at 0.0 and 1.0 ns in Fig. 1). Pursuing MD simulations for up to 10 ns, we find that the GB continues to deform and Fe atoms diffuse. Moreover, using a free boundary condition along the z axis for this system leads to the formation of a perfect crystal after 5 ns.

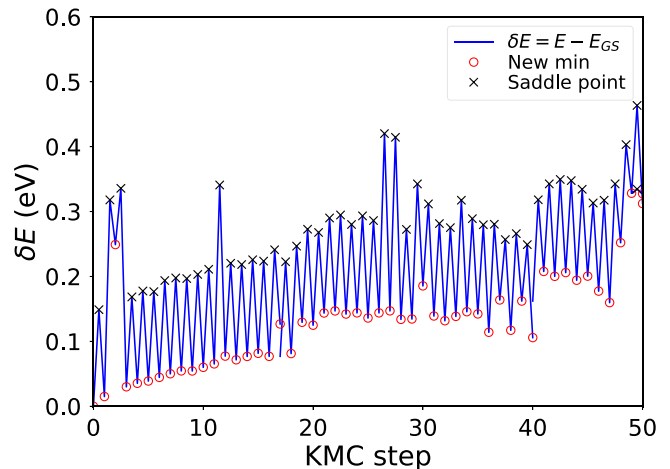


FIG. 2. K-ART evolution starting from an ideal $109.53^\circ \langle 110 \rangle$ GB structure without prior MD. The first 50 KMC steps are shown. Red circles represent local minima, black crosses the saddle points and the blue is guide to the eye. All energies are measured with respect to that of the initial configuration.

One-ns MD simulations are also launched on the four GBs with 1 C atom inserted at the GB. No diffusion is observed with the three lowest angle GBs as the C atom vibrates around their initial positions. These final configurations are used as input for the KMC simulations.

For the $109.53^\circ \langle 110 \rangle$ GB, large movements of the GB around the C atom are observed, with the impurity providing pinning similar to the Zener effect (pinning is observed both with periodic boundary conditions and with a free boundary in z). k-ART simulations launched from two configurations for this angle, one obtained after an MD run at 600 K and the other starting from the perfect GB structure (i.e., without any prior MD simulation) confirm that Fe atoms surrounding the GB can easily jump by crossing barriers with an average energy around ~ 0.1 eV, much lower than the energy barriers associated with C diffusion as is shown in Fig. 2. Because the kinetics of this system is dominated by the low-energy barriers associated with motion of an unstable GB at 600 K, we focus the rest of this paper on the remaining three GBs.

B. Stability of the GB over large time scales

We turn to the characterization of the long-time stability for the three remaining pure GBs. k-ART simulations are launched on the three lowest-angle GB systems, running about 200 steps, for total simulation times between 0.6 s and 1.2×10^{21} s, respectively. The minimum and barrier energies as well as the square displacements SD for the $18.93^\circ \langle 100 \rangle$ and the $70.53^\circ \langle 110 \rangle$ GBs are plotted in Fig. 3 as a function of time. Since, as can be seen in Fig. 1, the $85.91^\circ \langle 100 \rangle$ GB shows atomic environments very similar to that of the $18.93^\circ \langle 100 \rangle$ GB, leading to a very similar, but slower kinetics. Hence, simulation results for the long-time stability for the $85.91^\circ \langle 100 \rangle$ GB are not presented here.

As shown in Fig. 3, the $18.93^\circ \langle 100 \rangle$ system does not evolve significantly over time, the dynamics features are characterized by hops between the ground state and unstable higher energy states located 1.4 to 1.6 eV above the ground state. These

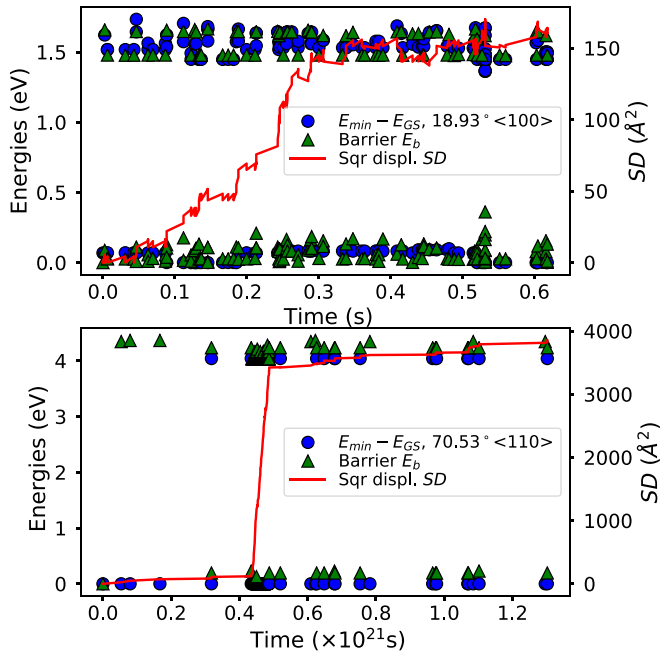


FIG. 3. Long-time evolution of minimum and barrier energies, and square displacement SD for (top) the $18.93^\circ \langle 100 \rangle$ and (bottom) $70.53^\circ \langle 110 \rangle$ GB systems. Blue dots: energy measured from the ground state (initial state, here); green dots: energy barrier; and red line: total square displacement.

high-energy states are very unstable and require crossing low barrier, about 0.1 eV, to get back to the ground state. The first half of the simulation (about 0.3 s as seen in Fig. 3) shows an apparent diffusion due to rearrangements of Fe atoms in the GB that does lead to a structural evolution. For example, some Fe atoms at the GB, represented in blue and evidenced by the red circle in Fig. 1, can jump back and forth into the free volume at the center of the circle. Since events for the $85.91^\circ \langle 100 \rangle$ GB are similar to this GB, no kinetic simulation was performed on the $85.91^\circ \langle 100 \rangle$ system and a single k-ART step was done to establish the energy landscape around the relaxed minimum. We find that the lowest barrier that needs to be crossed during the Fe atom hops is 2.3 eV indicating a much slower evolution in the $85.91^\circ \langle 100 \rangle$ system than in the $18.93^\circ \langle 100 \rangle$ one.

The pure Fe $70.53^\circ \langle 110 \rangle$ GB is more stable than the two previously investigated GBs featuring an energy landscape where the states are separated by large barriers of ~ 4 eV. These barriers lead to shallow minima with inverse barriers of ~ 0.1 eV to return to the ground state. The diffusion observed in Fig. 3 is associated with the interchange of Fe atoms in the bulk or at the GBs, that does not result into structural rearrangement.

The GB evolution time scales observed in these three are between 4 and 25 orders of magnitude larger than the average ~ 35 ns time scale of C diffusion in the Fe crystal at 600 K, associated with a 0.815 eV migration energy according to our calculations. We can then safely focus on the diffusion of C in the rest of this paper for these three grain boundaries, while ignoring Fe diffusion at the GBs or in the bulk.

C. Diffusion and segregation of a C atom at GBs

Having characterized the GB stability over short and large time scales, we now turn to diffusion of C from the bulk to and into a GB. All runs begin with a C atom placed into the middle of the crystalline zone, at equal distance of the two GBs. Unbiased kinetic simulations are then launched, letting the C atom find a physically relevant diffusion pathway. Ten independent simulations are performed on the $18.93^\circ \langle 100 \rangle$ and $70.53^\circ \langle 110 \rangle$ systems. Since all runs sample the same energy surface and lead to the same states, only one representative simulation is discussed here for each of the two systems. Due to the large size the $85.91^\circ \langle 100 \rangle$ GB simulation box only one run has been performed on this system.

We start by analyzing the energy minima and saddle points evolution of the three systems at two representative intervals as a function of KMC steps as shown in Fig. 4, to help understand the overall kinetics as discussed below. In this figure, saddle points connecting two minima are plotted every half step. Each directly connected minimum is shown with an open circle. A minimum represented by a filled red symbol corresponds to a disconnected exit site from a basin: since the average internal kinetics of basin is solved analytically using the bac-MRM, it is not possible to identify a unique pathway connecting the basin entrance and exit. A discontinuity is observed, for example, at step 250 for $85.91^\circ \langle 100 \rangle$ GB (bottom panel).

At the onset of the simulation, in the bulk, diffusion is similar for the three GBs; in this first regime, the C atom diffuses randomly from the center to a GB by crossing barriers around 0.85 eV, slightly higher than for the perfect crystal due to long-range strain effects caused by the GBs. In the simulations selected here, GBs are reached around steps 51, 84, and 255, as seen in the right panels of Fig. 4 from top to bottom, respectively. Once the C arrives at a GB, we observe a second regime where it is trapped into a region energetically favorable for segregation, i.e., the system falls into a lower energy state associated with the GB.

The energy gained by the C migrating to the GB, associated with trapping, can be significant: the energy difference with the carbon in the bulk (indicated by the horizontal red line in the left panels) and the lowest configuration in the GB, $E_0 - E_{GS}$, equals 0.86, 0.32, and 0.93 eV, respectively, from the lowest to the highest GB angle. In two runs of the $18.93^\circ \langle 100 \rangle$ system, a lower ground state 1.02 eV below the energy of C at lattice was found, however this additional reduction in energy was due to Fe re-accommodation at the two GBs and does not affect the C position.

To return to the crystalline side, the C atom must cross significant effective barriers of 1.70, 1.13, and 1.53 eV, respectively, as measured from the ground state. Due to a trapping energy, $E_0 - E_{GS} = 0.32$ eV, return to the crystalline side is only observed for the $70.53^\circ \langle 110 \rangle$ GB (for example, the gray area around step 1030 in the right panel of the middle graph in Fig. 4 indicates one of the intervals where the C jump to lattice for a period of ~ 70 ns before moving back to the GB, this phenomenon is also observed in other intervals and other simulations of the same system).

Diffusion towards and into the GB depends on the local structural deformation. In the $70.53^\circ \langle 110 \rangle$ GB, diffusion generally takes place by crossing relatively low energy barriers

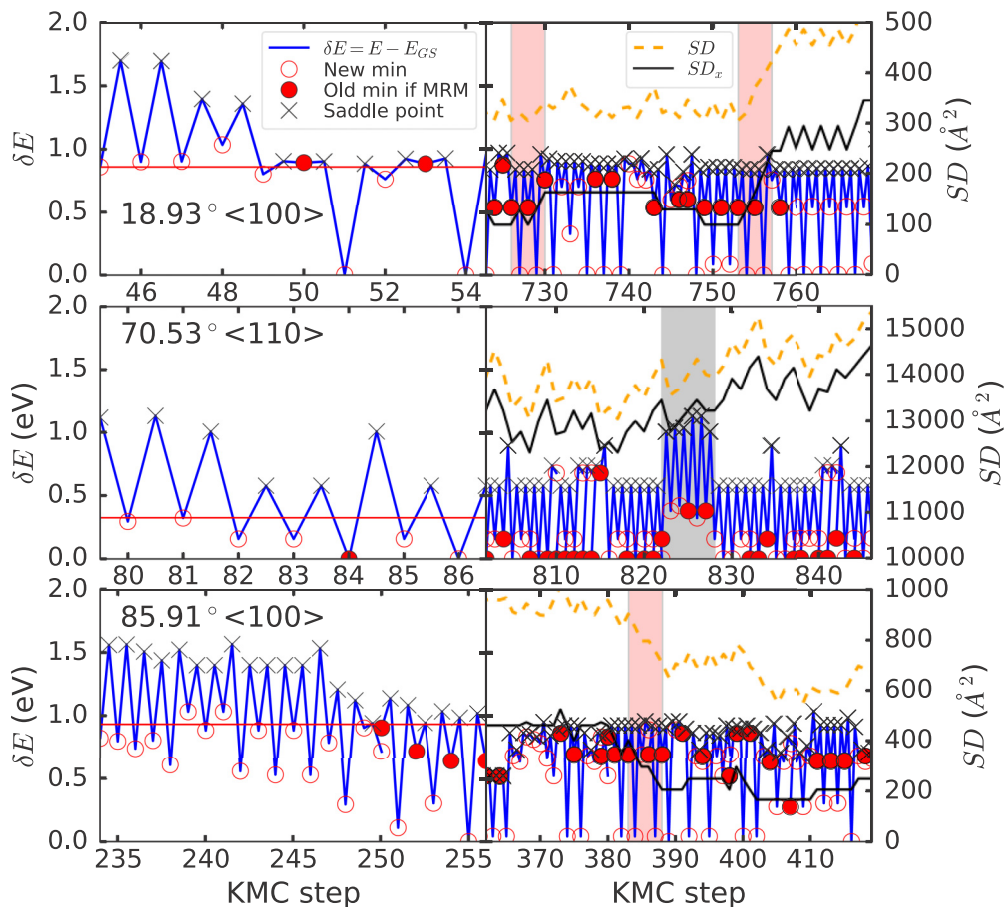


FIG. 4. Energy vs KMC steps for two intervals. Left, C approaching the GB from the bulk region. Horizontal red lines indicate the GS energy in the bulk, $E_0 - E_{GS}$, equal to 0.86, 0.32, and 0.93 eV from top to bottom. Right, regimes of C diffusion in the GB. The total square displacement SD and square displacement along x , SD_x , are also given. Pink shaded areas in top and bottom plots are intervals where the C atom moves into the GB plane while the gray band area, middle panel, indicates an interval in which the C atom returns to the crystalline side. Connected open dots indicate the exact trajectory. Filled circles indicate a discontinuity associated with an analytical solution of the flickering states using bac-MRM.

ranging from 0.42 to 0.60 eV, although the C atom also jumps infrequently over higher barriers with energy ranging from 0.74 to 0.94 eV. Diffusion is more complex in the $18.93^\circ \langle 100 \rangle$ and $85.91^\circ \langle 100 \rangle$ GBs, with multiple pathways observed. For example, two different pathways are highlighted in pink for the $18.93^\circ \langle 100 \rangle$ GB in the right panel of Fig. 4: in the first interval, diffusion from GS to GS requires crossing effective barriers of 0.84 eV (step 728) and 0.96 eV (step 730) while for the second pathway, diffusion takes place through barriers of 0.77 eV (step 755). Diffusion along the $85.91^\circ \langle 100 \rangle$ GB can also take place through several mechanisms. While many mechanisms are observed in Fig. 4, the mechanism highlighted around step 385 is associated with an effective barrier of 0.88 eV. Other mechanisms (not shown here) are observed with barriers of up to 1.2 eV.

The GB environment is energetically favorable to host C interstitials as demonstrated by the significant decrease in the total energies once the C atom reaches the GB. Furthermore, barriers for returning into the bulk are high and C diffusion is largely restricted to the interface: diffusion takes place mostly along 1 D channels for the $18.93^\circ \langle 100 \rangle$ and $85.91^\circ \langle 100 \rangle$ systems and can explore the full 2D GB plane for the 70.53°

$\langle 110 \rangle$ GB. Diffusion trajectories are shown in Fig. 5 over the GB in xy planes (insets show the projection along yz planes, perpendicular to the GB planes). An atomic view of GBs is given in Fig. 6, which shows the positions visited by the C atom as it diffuses along the various GBs.

C diffusion trajectories, such as those presented in Figs. 4–6, are complex and involve many flickering states, i.e., oscillations between states of similar energy that do not contribute to the diffusion. In Fig. 6, a black line connects flickering states occurring in the same yz plane for the $18.93^\circ \langle 100 \rangle$ and $85.91^\circ \langle 100 \rangle$ GBs, while they occur between yz plane for the $70.53^\circ \langle 110 \rangle$ GB. As explained above, to avoid getting the k-ART simulations trapped by flickers, we resolve the intrabasin kinetics by solving the average residence time analytically, creating a discontinuity in the trajectory as shown by the filled symbols in Fig. 4.

Full trajectories for the three systems are plotted as a function of time in Fig. 7. On the left axis, we show the energy barrier E_b , the segregation energy E_s and the basin threshold used in bac-MRM method and, on the right axis, the total, SD , and partial square displacements along each direction, SD_x , SD_y , and SD_z . SD_x and SD_y correspond

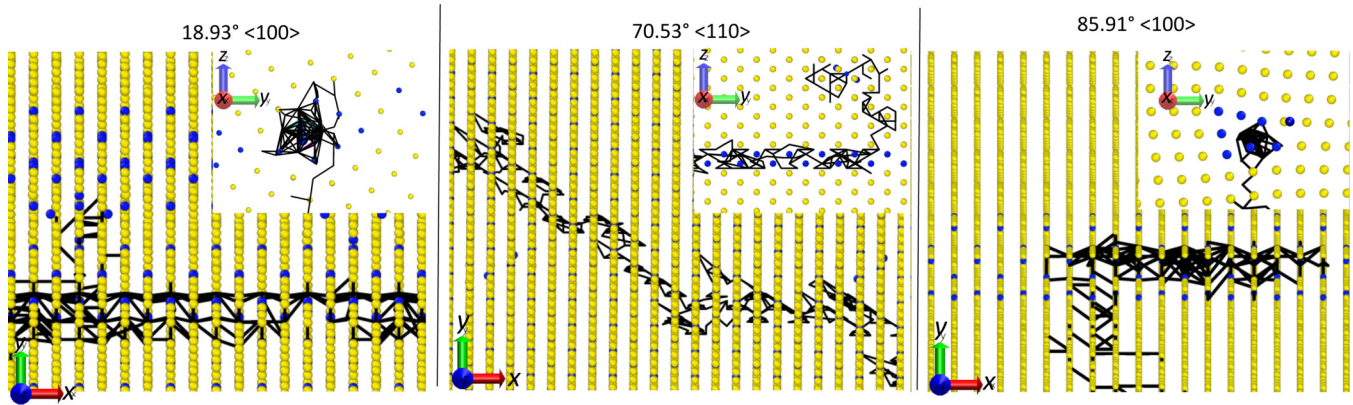


FIG. 5. Trajectory paths of a C atom at the GB planes xy . The Insets show the yz planes, perpendicular to the GBs planes. Fe atoms outside of bcc environment in the GBs are shown in blue. Note that some motion also takes place along the x direction and that multiples pathways can be projected on top of each other.

to displacement into GB-plane (see planes in Figs. 5 and 6) and SD_x is the displacement along the rotation axis $\langle 100 \rangle$ or $\langle 110 \rangle$. For the $18.93^\circ \langle 100 \rangle$ and $85.91^\circ \langle 100 \rangle$ systems, SD_x is the dominant direction of diffusion as motion is restricted to essentially a one-dimensional channel, as shown in the trajectories of Fig. 5. As a consequence of this 1D motion, the C atom oscillates around its initial position (as observed in SD , red lines) in the GB for these two systems. The situation is very different for the $70.53^\circ \langle 110 \rangle$ GB, where the 2D motion leads to a significant diffusion over a total time of $350 \mu s$.

C segregation refers to the local enrichment of this material in a matrix. It results as consequence of different diffusional processes [8]. A way to measure segregation is by considering the C segregation energy E_s , which is also plotted in Fig. 7. In the first KMC steps, the segregation energy is close to zero, as the C atom lies into the interstitial octahedral sites of the crystal side and does not feel the effect of the GB.

At the $18.93^\circ \langle 100 \rangle$ GB, C segregates easily, as most states have negative or close to zero segregation energies and can bind to sites with energies of up to 0.86 eV [as seen from $(E_0 - E_{GS})$ plot]. The energy difference between lower and higher states at the GB is around ~ 1.2 eV, in agreement with the barriers observed. A similar physics is observed in the

$85.91^\circ \langle 100 \rangle$ GB. For both systems, the higher energy states correspond to states at the border of the crystalline side. At the $70.53^\circ \langle 110 \rangle$ GB, the plot of E_s in Fig. 7 shows that the C atom jumps between bounded (E_s is negative) and repulsive (E_s is positive) energy states. These states are separated by large barriers of up to 1.0 eV, as discussed in the previous paragraph.

For the $18.93^\circ \langle 100 \rangle$ and $85.91^\circ \langle 100 \rangle$ GBs, Fig. 7 shows larger barrier energies inside the GBs than inside the bcc lattice (this is also true for the $70.53^\circ \langle 110 \rangle$ GB). In both systems, the C atom may find large barriers of up to 1.2, 1.0, and 1.1 eV, respectively, that have a direct effect in the time step.

Details of the dynamics evolution are provided in Fig. 8. This figure shows the instantaneous time step and its evolution averaged over 20 steps in parallel with the total SD for the three systems. For the $18.93^\circ \langle 100 \rangle$ and $85.91^\circ \langle 100 \rangle$ GBs, diffusion at the GB is slow, with time steps between $0.1 \mu s$ and $1.0 \mu s$ on average, corresponding to effective barriers up to 1.0 and 1.2 eV, compared with 0.85 eV in the bulk side. While lower barriers are also visible, it is clear that some of them connect flickering states and do not contribute to diffusion, as can be seen around steps 150, 300, 450, and 800, for example, for the $18.93^\circ \langle 100 \rangle$ system and steps 300 and 580 for $85.91^\circ \langle 100 \rangle$.

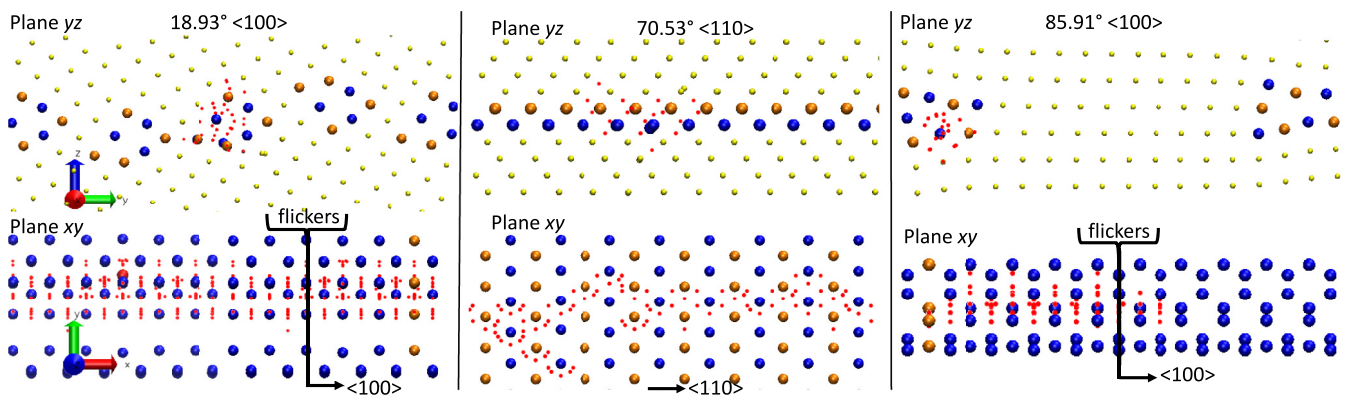


FIG. 6. Views of the positions visited by the C atom at the GBs (red dots). In top, yellow atoms represent crystalline positions that are removed, in the bottom panel, to simplify the diagram. Atoms in blue are at GBs. In the case of $70.53^\circ \langle 110 \rangle$, orange is used to distinguish the two alternating planes defined by a normal parallel to the rotation tilt axis. Flickering states along $\langle 100 \rangle$ planes are indicated by the red dots underlined by a black line.

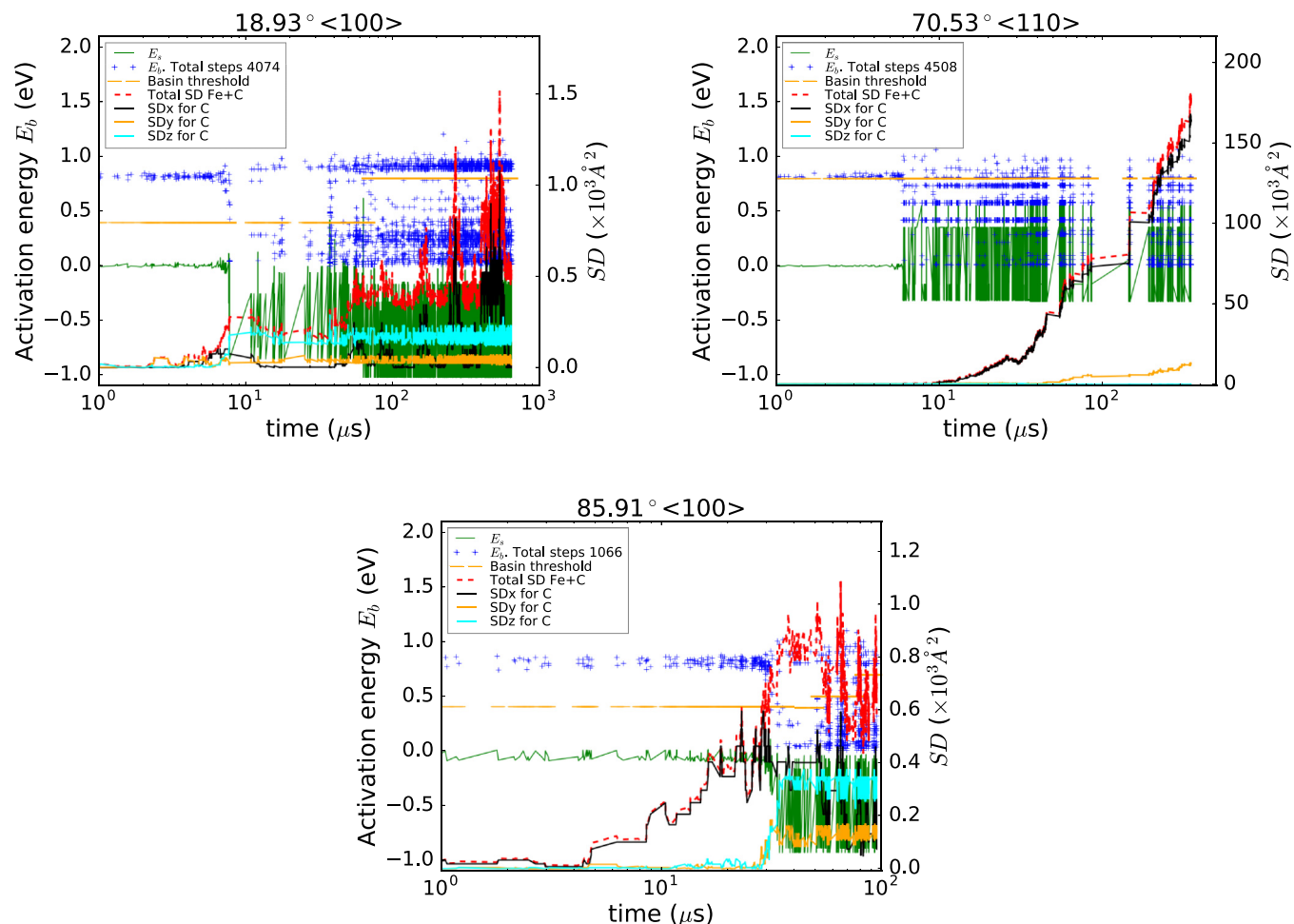


FIG. 7. Time evolution of C diffusion at the GBs with k-ART plotted on a logarithmic scale. Left axis: barrier energies E_b (blue crosses), segregation energy E_s (green lines), and the basin threshold energy (horizontal lines in orange), in eV. Right axis: total and partial square displacement SD , SD_x , SD_y , and SD_z in \AA^2 . Top left panel: $18.93^\circ \langle 100 \rangle$ GB; top right panel: $70.53^\circ \langle 110 \rangle$ GB; bottom panel: $85.91^\circ \langle 100 \rangle$ GB.

In some path intervals, diffusion is faster for the $70.53^\circ \langle 110 \rangle$ GB system, with typical time steps shorter at the GB than in the bulk, typically between $0.01 \mu\text{s}$ and $0.1 \mu\text{s}$ (this is the case of time steps shown in Fig. 8). However, there are intervals where time steps are up to $50 \mu\text{s}$, associated with barriers of $\sim 1.0 \text{ eV}$ (not shown in Fig. 8). Flickers are rarer for this system, preventing trapping and facilitating long-distance motion.

Long-range interactions can also affect the energies. For the $18.93^\circ \langle 100 \rangle$ system, for example, we observe an interaction between the two parallel grain boundaries (GB1 and GB2), situated 25.8 \AA from each other, where the C motion in GB1 leads to a Fe rearrangement in GB2 that lowers the energy by 0.17 eV below the ground state observed in GB1 before rearrangement (see the energies in Fig. 7 around time $60 \mu\text{s}$ and in detail around step 980 in Fig. 9). This phenomenon is observed in two of ten simulations, but is not observed in the pure Fe simulation, without C. We note that such effects can only be captured with k-ART as this algorithm takes full account of long-range elastic effects contrary to standard KMC approaches which often are done on rigid lattices.

D. Topologies and catalog

k-ART relies on a one-to-one correspondence between local topology and geometry imposed by the overall 3D structure and the interaction [37]. Thus, for each new topology found, a series of ART-nouveau searches is launched to identify all the possible events associated with this topology. k-ART assumes that all the atoms sharing the same topology label have the same generic events, with the exact barrier and atomic positions depending on the specific realization that can be recomputed when needed (this assumption is validated when specific events are reconstructed). All generic events are stored in a catalog and are used when a topology is identified again during the simulation, significantly reducing simulation costs. This approach avoids the need to construct all possible conformations from the onset as KMC steps advances, a task that would rapidly be impossible for our GB systems.

Figure 10 shows the evolution of the number of encountered topologies as well as the CPU-time spent for finding new topologies and exploring the event list as a function of KMC step. We observe a clear correspondence between the search for new topologies and the CPU time. Plateaus in the number of topologies indicate that the C atom evolves in an environment

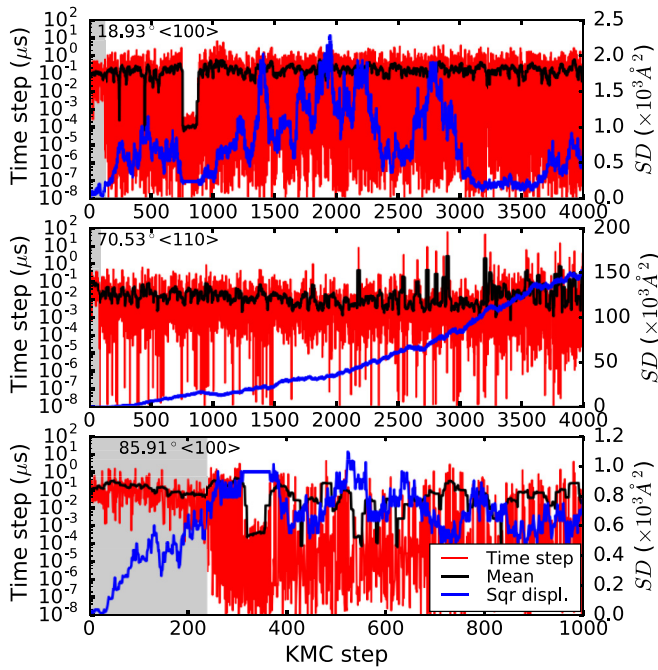


FIG. 8. Evolution of the systems as a function of KMC step. Left axis: instantaneous (red line) and average (black line) time step as a function of KMC step. Right axis: total square displacement (SD) (blue). The average time step is computed as moving average using a window of 20 steps. Gray areas correspond to movements into the crystalline side.

that has already been well characterized. At the end of the simulations for $18.93^\circ \langle 100 \rangle$ and $85.91^\circ \langle 100 \rangle$ systems, around 60 000 and 43 000 topologies are analyzed for new events over 4000 and 1000 KMC steps, respectively. The $70.53^\circ \langle 110 \rangle$ system is less complex and less expensive with around 1400 topologies analyzed over 4500 KMC steps. While this number of topologies appears large, it includes both topologies visited during the simulation and those found in connected minima that are never selected. It is therefore much smaller, as it is constructed only on a need basis, than would be required by incorporating all possible conformations from the simulation onset as done in standard KMC simulations.

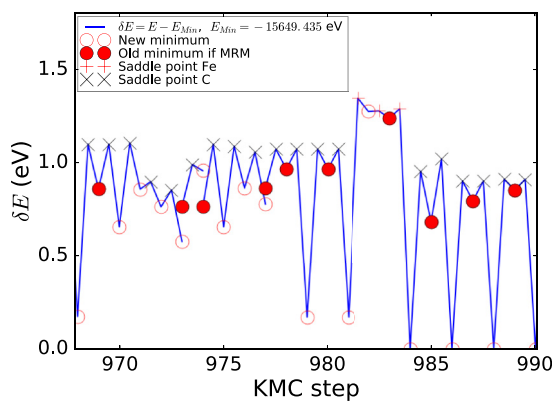


FIG. 9. (Left) Evolution of the $18.93^\circ \langle 100 \rangle$ system as a function of KMC step near the reorganization in GB2 due to the presence of a C atom in GB1: see events 980–985. (Right) The corresponding Fe-atom displacements to a new ground state (blue dots, right GB).

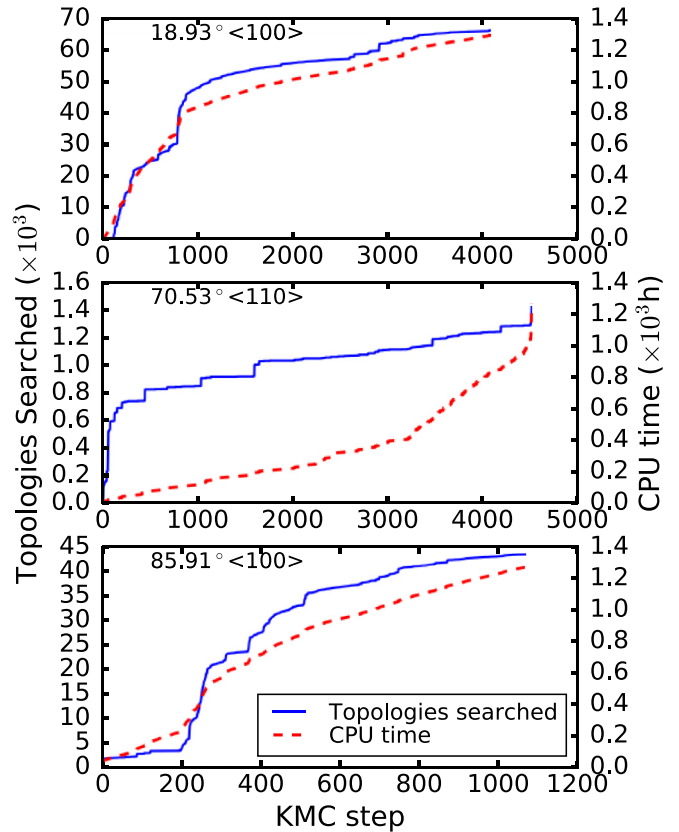
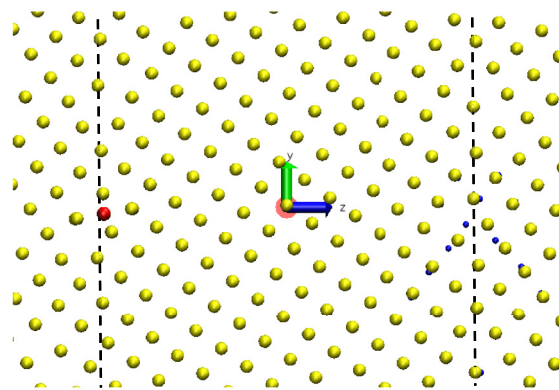


FIG. 10. Evolution of the number of searched topologies and CPU time (in hour) as a function of KMC step for typical run of three GBs. Top: $18.93^\circ \langle 100 \rangle$; middle: $70.53^\circ \langle 110 \rangle$; bottom: $85.91^\circ \langle 100 \rangle$.

E. Relations between barriers, minimum energies, and volumes

Despite the large number of topologies, most of them involve events similar in energy and nature that can be classified more efficiently, from a physical point of view, as a function of their energy and volume. The $70.53^\circ \langle 110 \rangle$ GB system is the poorest in terms of topologies with around $\sim 90\%$ per KMC step, but with only five geometrically different minimum energy states found at the GBs. In contrast, an analysis of the $18.93^\circ \langle 100 \rangle$ and $85.91^\circ \langle 100 \rangle$ GBs shows a wealth of



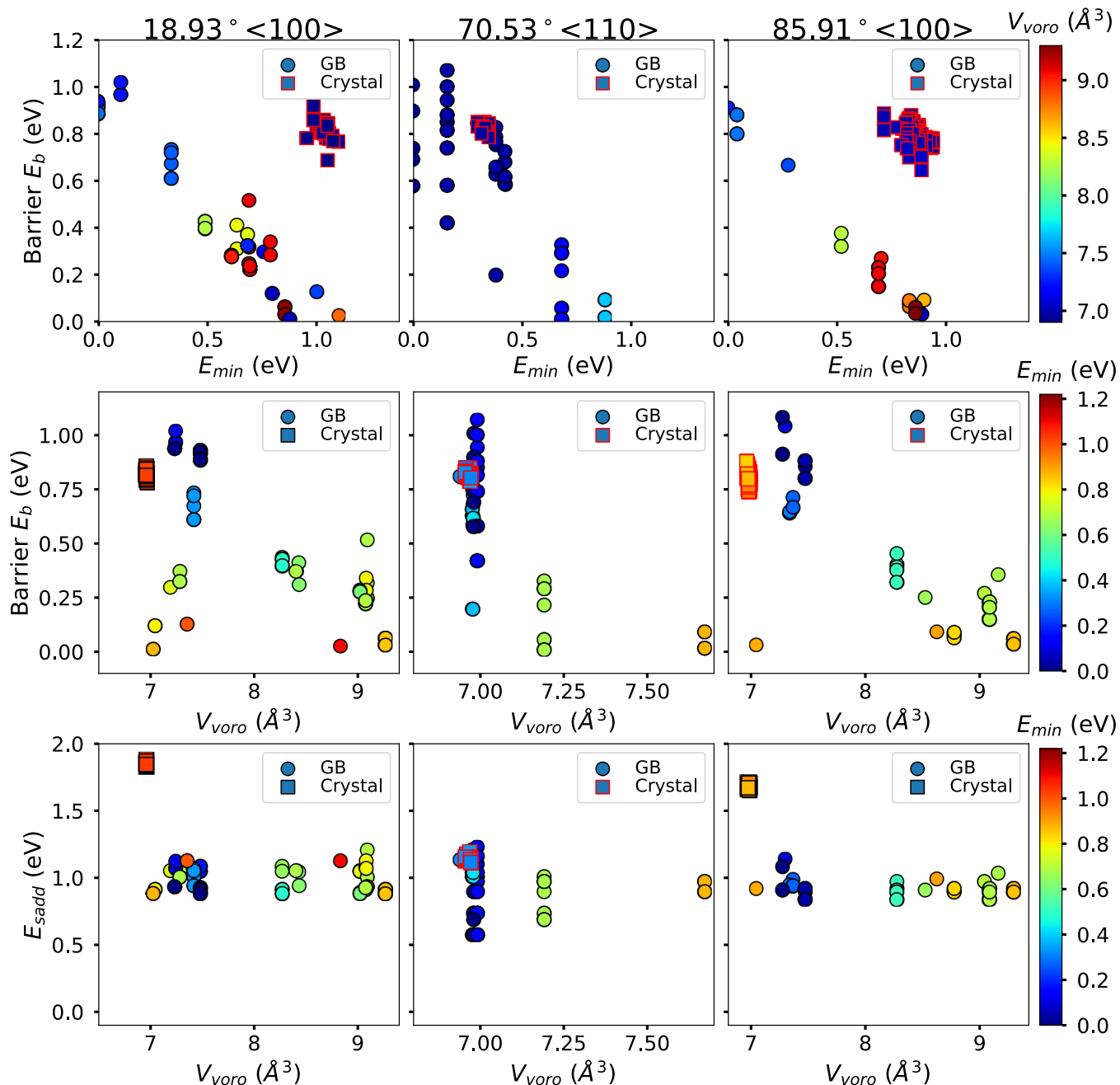


FIG. 11. Relations between energy barrier E_b , energy minimum E_{min} , energy saddle E_{sadd} , and Voronoi volume V_{voro} . To better see physical trends, flickering states and states that produce jumps into the same plane, perpendicular to direction of diffusion are removed. Squares are used for data corresponding to C in the bulk, whereas circles correspond to data obtained when the C atom is in the GB.

different topologies (up to 420 and 359 topologies per KMC step, respectively) with energies varying by up to 1.3 eV.

It is customary to link diffusion barriers with the free volume available to the impurity. Figure 11 examines this correlation for the three GBs by plotting the barrier, minimum energy, saddle energy and the Voronoi volume associated with the C impurity. To better focus on the diffusion processes, flickering states and states that correspond to jumps into the same plane have been removed, leaving only moves associated with displacements at the GB larger than 1.0 Å along the direction of diffusion. The top-row plots demonstrate a significant correlation between the minimum and the barrier

energy at the GB. This correlation is explained by the fact that a strong local deformation increases the local energy mostly by weakening the interaction. This is particularly clear when the sites associated with the perfect crystal (square symbols in Fig. 11) are ignored.

Additional information about the physics behind barriers can be obtained by plotting the barrier and saddle energies as function of the Voronoi volume (see Fig. 11 middle- and bottom-row plots). Barrier energies show a clear trend with the free volume surrounding the impurity, as characterized by its associated Voronoi volume, with the higher barriers found at the lower volumes. However, there is wide scattering in the

barriers of impurities with small Voronoi volume, a scattering particularly notable for the first two GBs. For these three systems, the Voronoi volume occupied by the C at the GB varies by up to 34%, from 6.96 to 9.30 \AA^3 (the lowest value represents the volume occupied by a C atom in the crystalline lattice). The color scale for these plots also indicate that the strain for the associated minimum bears is somewhat correlated with the Voronoi volume, indicating that a larger free volume at the local minimum is more likely to be caused by high strain on the impurity. Moreover, larger volumes are generally associated with larger excited energy states (i.e., configuration states with higher energy than the ground state) and smaller energy barriers. For example, in the $18.93^\circ \langle 100 \rangle$ and the $85.91^\circ \langle 100 \rangle$ systems, states with energy between 0.6 and 1.0 eV have volumes around $\sim 9.0 \text{ \AA}^3$ and are very unstable, with barrier of 0.05 eV, at most. However, the trend is far from perfect as can be seen in Fig. 11. As for the $70.53^\circ \langle 110 \rangle$ GB, there are only three different volumes of 6.90, 7.19, and 7.67 \AA^3 but each shows a distribution of the E_{\min} .

The importance of strain over volume is made clearer when we look at the bottom-row of plots, which present the saddle energy measure from the lowest-energy configuration found along the diffusion pathway, which allows us to identify the long-range effective diffusion barrier, as a function of its Voronoi volume. The lowest energy states with respect to the GS, from left to right are found to be 0.89 eV, 0.56 eV and 0.84 eV. For the $18.93^\circ \langle 100 \rangle$ and $85.91^\circ \langle 100 \rangle$ GS, these values are higher than the bulk barrier diffusion. This is not the case for the $70.53^\circ \langle 110 \rangle$ GB system, which shows an effective diffusion barrier at the GB that is considerably lower than in the bulk. The lowest saddle point corresponds to a Voronoi volume close that of the perfect crystal and turns out to be the dominant diffusion mechanism for C. Nevertheless, this system shows several minimum and barrier energies associated with a number of different topologies that display similar volume but different minima and barrier energies to leave them. Interestingly, the three bottom-row plots show almost constant saddles energies as a function of Voronoi volume, which suggests that the elastic deformation that leads to the correlation found in the top-row graphs is not caused by volume but involves more complex bounding terms.

IV. DISCUSSION

The use of k-ART allows a characterization of the energy landscape at a level that goes well beyond molecular dynamics or static simulations as it provides detailed information regarding the GB evolution and the complex diffusion pathways of C around them. In molecular static simulations, segregation energy can be studied as a function of the distance to the GB center [19]. However, the plots obtained are complicated to analyze, because of the diversity of topologies at GBs. In contrast, k-ART selects only the most probable configurations at a given temperature, therefore producing more readable information of the relevant energy landscape, as shown in Fig. 4. Indeed, k-ART can recover the full C diffusion paths in the presence of a GB at an experimentally relevant temperature. This is in contrast to molecular statics where paths must be

guessed from the minimum energies computed, without taking barriers into account.

Molecular dynamics can also be used to characterize GB systems. These characterizations are essential to establish what structures are really relevant at finite temperatures; however, MD alone does not provide all the necessary information regarding the energy landscape and long-time kinetics.

Out of the four grain boundaries studied, we show, using MD and k-ART, that the 109.53° GB (found in literature as $\Sigma 3(111)$) is unstable at 300 K (and 600 K), with barriers as low as ~ 0.1 eV, much below those associated with C diffusion. In this system, impurities do not dominate diffusion but act, rather, as pinning centers. Our results allow us to predict that in a pure polycrystalline-Fe sample, this GB would be wiped out by small variations of pressure and temperature in favor of other grains, unless it was stabilized by an impurity. In contrast, the three other GBs are very stable, with energy barriers of many eV, significantly limiting the evolution of these systems.

With the full k-ART assisted characterization of the energy barriers and diffusion pathways, we can also better understand the role of GBs for the diffusion of impurities. Based on relatively old experiments [13], it is generally assumed that diffusion at a GB is faster than in the bulk lattice, often by many orders of magnitude. As discussed by Teus *et al.* [12] this conclusion is based on improper analysis that applies vacancy migration observations to interstitials. Indeed, for interstitials, Teus *et al.* found discrepancies between other authors' experiments and their own study and proposed that the low diffusivity of interstitial atoms at GBs can be explained by the disappearance or the drastic decrease of the elastic term in the gradient of chemical potential due to their capture by GBs. They also argued that the low diffusivity of C atoms at GBs is caused by the strong affinity of interstitials for voids or vacancies (e.g., the effective barrier to move the complex vacancy-C is around ~ 1.7 eV [7]). In this case, GBs can be considered as a mixture of vacancies and C atom interstitials forming complexes that barely move an argument also applicable to dislocations as they can be considered as chain of vacancies. Teus *et al.* also explain the problems with Bockstein *et al.* results [13] by the role of surfaces on C content differences between the bulk and the GB that can be interpreted as a faster diffusion of C atoms along the GBs.

Oudriss *et al.* [29] also take objection with the standard characterization and observe two different behaviors for H diffusion in Ni: when $\Sigma > 29$ (general or random GBs), they observe acceleration of the diffusion by GB while when $\Sigma < 29$ (special GBs), they observe impurity trapping. They conclude that trapping is due to larger volumes and vacancies at the Ni GBs, while acceleration can be explained by a disordered structure, where diffusion is faster because of a large excess of free volume. In general, trapping and diffusion depend on several factors like "the grain size, the probability of grain boundary connectivity, the grain boundary energy, and the excess of free volume" [29]. We showed in Ref. [57] that C diffusion at the surfaces of bcc-Fe is faster than in the bulk, and for the GBs we investigated, it is the opposite. The detailed characterization of the energy landscape provided by k-ART supports these observations and offers a more precise and

subtle explanation of the effect of grain boundaries on the diffusion of impurities.

First, most theoretical analyses of C diffusion at GBs associate lower diffusion barriers at these interfaces with a GB-dominated diffusion. We find, rather, that this domination is not due to lower effective diffusion barriers at the GB, as we observe both lower and higher C diffusion barriers at the GBs with respect to bulk. Impurity diffusion nevertheless takes place at the GB because even higher barriers are encountered for an interstitial to move from the GB to the bulk. GB diffusion dominates, therefore, because these regions represent an energetic sink from which impurities can rarely escape to move back into the bulk, even if diffusion barriers are lower in the crystalline environment, leading to a higher impurity concentration at the GB and, therefore, an interface-dominated overall diffusion. Our results clearly show that the GB is a preferred route not because a C atom moves faster into it—as higher barriers can be found inside—but because GBs constitute regions with a lower energy for the total system.

Finally, a characterization of the Voronoi volumes associated with energy minima and diffusion barriers for C atoms at the GBs demonstrates that, contrary to what has been proposed [29], there is no strong correlation between free volume and diffusion barriers. As we show, although the largest free volumes tend to be associated with more unstable states, the smallest volumes allow low as well as high diffusion barriers. This is particularly clear when plotting the energy at the saddle points measured from the lowest-energy state on the diffusion pathway, which shows an almost constant value as a function of the Voronoi volume. Understanding impurity diffusion pathways and kinetics requires, therefore, specific characterization of each environment and no rule of thumb can be established from general knowledge of the GB such as its type or desorientation.

V. CONCLUSIONS

There has been much debate as to the role of GBs for impurity diffusion. For a long time, it was believed that GBs provide rapid pathways for impurities, particularly for C in bcc metals. This simple image was criticized recently by a number of groups [12,29] who suggested that diffusion could be enhanced or reduced by the presence of these interfaces, and that their overall behavior was linked to free volume. Using the k-ART—an off-lattice kinetic Monte Carlo algorithm with on-the-fly catalog building, which fully incorporates strain effects—we revisited this question by considering long-time C diffusion near different GB at the experimentally relevant temperature of 600 K. This technique allowed us to generate detailed kinetics while constructing the full energy landscape around each visited local minimum.

We showed that not all GBs identified statically are stable over large time scales. This is the case of the $\Sigma 3(111)\theta = 109.53^\circ(100)$ GB, where the migration barriers of Fe atoms are smaller than those of the C atom (around 0.1 eV), therefore the C impurity can act as a pinning center for the GB migration and C diffusion is not observed. There are many papers about this particular case and all are related to static properties, its dynamics at other temperatures different to 0 K has not been studied before according to the bibliography found.

We also showed that for the three stable GBs, C diffuses and remains largely trapped at the GBs, with energy gains ranging between 0.3 and 0.9 eV with respect to the bulk energy. Diffusion along the GB, however, is determined by the effective barriers between the lowest-energy states in the GB. These can be either lower or higher than for bulk C diffusion, ranging from ~ 0.5 to ~ 1.2 eV depending on the GB. Because of trapping, however, the impurity is lead through the GB irrespective of these barriers. Whether slower or faster than in the bulk, impurity diffusion takes place in the GB. Depending on the GB type, C paths can be unidimensional or two dimensional. More precisely, C diffusion takes place mostly along 1D channels for the $18.93^\circ(100)$ and $85.91^\circ(100)$ systems and it can explore the full 2D GB-plane for the $70.53^\circ(110)$ GB. Faster than bulk pipe diffusion along GBs cannot, therefore, be postulated as a general rule. The GB is a preferred route not because a C atom moves faster into it—as higher barriers can be found inside—but because GBs constitute regions with a lower energy for the total system. The diffusivity is not necessarily faster and in our case, it is slower for $18.93^\circ(100)$ and $85.91^\circ(100)$ systems. Our results demonstrate the importance of extensively characterizing the kinetic pathways and associated energy landscapes to understand the fundamental behavior of these complex materials by focusing, in particular, on the relevant time scale. In this paper, this approach has allowed us to provide a precise answer to a debate that has been going on for decades in metallurgy, helping to gain a much deeper understanding of the fundamental mechanisms associated with impurity diffusion in metals.

Detailed characterization of the diffusion mechanism shows finally, that, contrary to what was proposed, the impurity diffusion barriers are not strongly correlated with the available free volume. Apparently, the kinetics depends much more subtly on the local environment and should be computed directly. However, the saddle energies, measured from the lowest-energy state are largely independent of the free volume surrounding the impurity. This suggests that the effective barriers for diffusion are limited to a fixed range of energies. To find these energy ranges requires additional simulations with several GBs structures. Clearly, additional simulations are needed to assess how other defects such as vacancies and substitutional atoms diffuse at GBs; simulations are underway.

ACKNOWLEDGMENTS

This work is supported by the Qatar National Research Fund (QNRF) through the National Priorities Research Program (NPRP 6 -863-2-355). This work has been supported by the Canada Research Chairs program and by grants from the Natural Sciences and Engineering Research Council of Canada (NSERC). We are grateful to *Calcul Québec/Compute Canada* (CQ/CC) for generous allocations of computer resources. This project has received funding from the Euratom research and training programme 2014–2018 under Grant Agreement No. 661913. This text reflects only the author's view and the Commission is not responsible for any use that may be made of the information it contains.

The k-ART package is available for distribution by contacting the authors.

- [1] G. Y. Lai, *High-Temperature Corrosion and Materials Applications* (ASM International, Materials Park, Ohio, 2007).
- [2] R.B. Anderson, *The Fischer-Tropsch Synthesis* (Academic Press, New York, 1984).
- [3] P. Yvon and F. Carré, *J. Nucl. Mater.* **385**, 217 (2009).
- [4] N. A. Vinogradov, A. A. Zakharov, V. Kocevski, J. Rusz, K. A. Simonov, O. Eriksson, A. Mikkelsen, E. Lundgren, A. S. Vinogradov, N. Mårtensson, and A. B. Preobrajenski, *Phys. Rev. Lett.* **109**, 026101 (2012).
- [5] A. J. Page, F. Ding, S. Irle, and K. Morokuma, *Rep. Prog. Phys.* **78**, 036501 (2015).
- [6] S. Riikonen, A. V. Krashennnikov, and R. M. Nieminen, *Phys. Rev. B* **82**, 125459 (2010).
- [7] O. A. Restrepo, N. Mousseau, F. El-Mellouhi, O. Bouhali, M. Trochet, and C. S. Becquart, *Comput. Mater. Sci.* **112**, 96 (2016).
- [8] H. Mehrer, *Diffusion in Solids Fundamentals, Methods, Materials, Diffusion-Controlled Processes* (Springer, Berlin, Heidelberg, 2007).
- [9] R. W. Powers and M. V. Doyle, *J. Appl. Phys.* **30**, 514 (1959).
- [10] G. Tibbetts, *J. Appl. Phys.* **51**, 4813 (1980).
- [11] H. Fujii and S. Tsurekawa, *Phys. Rev. B* **83**, 054412 (2011).
- [12] S. M. Teus, V. F. Mazanko, J.-M. Olive, and V. G. Gavriljuk, *Acta Mater.* **69**, 105 (2014).
- [13] S. Z. Bockstein, M. A. Gubareva, I. E. Kontorovich, and L. M. Moroz, *Met. Sci. Heat Treat. Metals* **3**, 6 (1961).
- [14] M. Wu, J. Gu, and Z. Jin, *Scr. Mater.* **107**, 75 (2015).
- [15] O. Kapikranian, H. Zapolsky, C. Domain, R. Patte, C. Pareige, B. Radiguet, and P. Pareige, *Phys. Rev. B* **89**, 014111 (2014).
- [16] R. Wu, A. J. Freeman, and G. B. Olson, *Phys. Rev. B* **53**, 7504 (1996).
- [17] W. T. Geng, J.-S. Wang, and G. B. Olson, *Science* **309**, 1677 (2005).
- [18] M. Yamaguchi, M. Shiga, and H. Kaburaki, *Science* **307**, 393 (2005).
- [19] M. A. Tschopp, K. N. Solanki, F. Gao, X. Sun, M. A. Khaleel, and M. F. Horstemeyer, *Phys. Rev. B* **85**, 064108 (2012).
- [20] J. Askill, *Tracer Diffusion Data for Metals, Alloys, and Simple Oxides* (Springer, US, New York, 1970), Chap. 1.
- [21] P. Shewmon, in *Diffusion in Solids* (Wiley, Hoboken, NJ, 1989), pp. 191–222.
- [22] A. Ishii, J. Li, and S. Ogata, *PLoS ONE* **8**, 1 (2013).
- [23] A. Ishii, S. Ogata, H. Kimizuka, and J. Li, *Phys. Rev. B* **85**, 064303 (2012).
- [24] Y. A. Du, J. Rogal, and R. Drautz, *Phys. Rev. B* **86**, 174110 (2012).
- [25] A. M. Brass and A. Chanfreau, *Acta Mater.* **44**, 3823 (1996).
- [26] B. Ladna and H. K. Birnbaum, *Acta Metall.* **35**, 2537 (1987).
- [27] S.-M. Lee and J.-M. Lee, *Metall. Trans. A* **17**, 181 (1986).
- [28] T. M. Harris and R. M. Latanision, *Metall. Trans. A* **22**, 351 (1991).
- [29] A. Oudriss, J. Creus, J. Bouhattate, E. Conforto, C. Berziou, C. Savall, and X. Feaugas, *Acta Mater.* **60**, 6814 (2012).
- [30] A. Pedersen and H. Jónsson, *Acta Mater.* **57**, 4036 (2009).
- [31] M. Herbig, D. Raabe, Y. J. Li, P. Choi, S. Zaeferrer, and S. Goto, *Phys. Rev. Lett.* **112**, 126103 (2014).
- [32] A. P. Sutton and V. Vitek, *Philos. Trans. R. Soc. London A* **309**, 55 (1983).
- [33] G. H. Bishop and B. Chalmers, *Scr. Metall.* **2**, 133 (1968).
- [34] G. H. Bishop and B. Chalmers, *Philos. Mag.* **24**, 515 (1971).
- [35] N. Mousseau, L. K. Béland, P. Brommer, F. El-Mellouhi, J.-F. Joly, G. K. N'Tsouaglo, O. Restrepo, and M. Trochet, *Comput. Mater. Sci.* **100**, 111 (2015).
- [36] L. K. Béland, P. Brommer, F. El-Mellouhi, J.-F. Joly, and N. Mousseau, *Phys. Rev. E* **84**, 046704 (2011).
- [37] F. El-Mellouhi, N. Mousseau, and L. J. Lewis, *Phys. Rev. B* **78**, 153202 (2008).
- [38] S. Plimpton, *J. Comput. Phys.* **117**, 1 (1995).
- [39] LAMMPS web site, <http://lammps.sandia.gov/index.html>
- [40] G. T. Barkema and N. Mousseau, *Phys. Rev. Lett.* **77**, 4358 (1996).
- [41] R. Malek and N. Mousseau, *Phys. Rev. E* **62**, 7723 (2000).
- [42] E. Machado-Charry, L. K. Béland, D. Caliste, L. Genovese, T. Deutsch, N. Mousseau, and P. Pochet, *J. Chem. Phys.* **135**, 034102 (2011).
- [43] H. Eyring, *Chem. Rev.* **17**, 65 (1935).
- [44] M. G. Evans, *Trans. Faraday Soc.* **31**, 875 (1935).
- [45] K. J. Laidler and M. C. King, *J. Phys. Chem.* **87**, 2657 (1983).
- [46] A. F. Voter, *Phys. Rev. B* **34**, 6819 (1986).
- [47] B. D. McKay, *Congr. Numer.* **30**, 45 (1981).
- [48] B. D. McKay and A. Piperno, *J. Symb. Comput.* **60**, 94 (2014).
- [49] C. Becquart, J. Raulot, G. Bencteux, C. Domain, M. Perez, S. Garruchet, and H. Nguyen, *Comput. Mater. Sci.* **40**, 119 (2007).
- [50] R. Veiga, C. Becquart, and M. Perez, *Comput. Mater. Sci.* **82**, 118 (2014).
- [51] M. Mendeleev, S. Han, D. Srolovitz, G. Ackland, D. Sun, and M. Asta, *Philos. Mag.* **83**, 3977 (2003).
- [52] P. Lejcek, *Grain Boundary Segregation in Metals* (Springer-Verlag, Berlin, Heidelberg, 2010).
- [53] P. Brommer, L. K. Béland, J.-F. Joly, and N. Mousseau, *Phys. Rev. B* **90**, 134109 (2014).
- [54] B. Puchala, M. L. Falk, and K. Garikipati, *J. Chem. Phys.* **132**, 134104 (2010).
- [55] D. J. Young and J. Zhang, *ECS Trans.* **16**, 3 (2009).
- [56] A. Wiltner, Ch. Linsmeier, and T. Jacob, *J. Chem. Phys.* **129**, 84704 (2008).
- [57] O. A. Restrepo, C. S. Becquart, F. El-Mellouhi, O. Bouhali, and N. Mousseau, *Acta Mater.* **136**, 303 (2017).